



## Full Length Article

# Enhancing hydrogen storage performance of MgH<sub>2</sub> with hollow Bi<sub>2</sub>Ti<sub>2</sub>O<sub>7</sub> catalyst: Synergistic effects of Bi<sub>2</sub>Mg<sub>3</sub> alloy phase and Ti polyvalency

Xiaoying Yang<sup>a</sup>, Xinqiang Wang<sup>a,\*</sup>, Ruijie Liu<sup>a</sup>, Yanxia Liu<sup>a</sup>, Zhenglong Li<sup>a</sup>, Wengang Cui<sup>a</sup>, Fulai Qi<sup>a</sup>, Yaxiong Yang<sup>a</sup>, Jian Chen<sup>a,\*</sup>, Hongge Pan<sup>a,b,\*</sup>

<sup>a</sup>Institute of Science and Technology for New Energy, Xi'an Technological University, Xi'an, 710021, PR China

<sup>b</sup>School of Materials Science and Engineering State Key Laboratory of Clean Energy Utilization, Zhejiang University, Hangzhou, 310027, PR China

Received 26 February 2025; received in revised form 30 April 2025; accepted 7 June 2025

Available online xxx

## Abstract

The role of catalysts in enhancing the hydrogen storage kinetics of the Mg/MgH<sub>2</sub> system is pivotal. However, the exploration of efficient catalysts and the underlying principles of their design remain both a prominent focus and a significant challenge in current research. In this study, we present a bimetallic oxide of Bi<sub>2</sub>Ti<sub>2</sub>O<sub>7</sub> hollow sphere as a highly effective catalyst for MgH<sub>2</sub>. As a result, the Bi<sub>2</sub>Ti<sub>2</sub>O<sub>7</sub>-catalyzed Mg/MgH<sub>2</sub> system lowers the hydrogen desorption initiation temperature to 194.3 °C, reduces the peak desorption temperature to 245.6 °C, decreases the dehydrogenation activation energy to 82.14 kJ·mol<sup>-1</sup>, and can absorb 5.4 wt. % of hydrogen within 60 s at 200 °C, demonstrating outstanding hydrogen ab/desorption kinetics, compared to pure MgH<sub>2</sub>. Additionally, it can maintain a high hydrogen capacity of 5.2 wt. %, even after 50 dehydrogenation cycles, showing good cycle stability. The characterization results show that the high-valent Bi and Ti in Bi<sub>2</sub>Ti<sub>2</sub>O<sub>7</sub> are reduced to their low-valent or even zero-valent metallic states during the dehydrogenation and hydrogenation process, thus establishing an *in-situ* multivalent and multi-element catalytic environment. Density functional theory calculations further reveal that the synergistic effects between Bi and Ti in the Bi-Ti mixed oxide facilitate the cleavage of Mg-H bonds and lower the kinetic barrier for the dissociation of hydrogen molecules, thereby substantially enhancing the kinetics of the Mg/MgH<sub>2</sub> system. This study presents a strategic method for developing efficient catalysts for hydrogen storage materials by harnessing the synergistic effects of metal elements.

© 2025 Chongqing University. Publishing services provided by Elsevier B.V. on behalf of KeAi Communications Co. Ltd.

This is an open access article under the CC BY-NC-ND license (<http://creativecommons.org/licenses/by-nc-nd/4.0/>)

**Keywords:** Hydrogen storage; MgH<sub>2</sub>; Bimetallic oxide; Catalysts; Synergistic effects.

## 1. Introduction

Energy serves as a fundamental material cornerstone for the survival and advancement of human society. As global progress accelerates and living standards continue to rise, the escalating energy demand coupled with the gradual depletion of fossil fuels presents an urgent and profound challenge that the world must confront [1–5]. In order to meet future energy demands, particularly in the transportation sector, which

accounts for nearly 60 % of global energy consumption, there is an immediate need to identify green, efficient alternatives to traditional fossil fuels [6–10]. Among the various potential sources of alternative energy, hydrogen stands out as a premier option, owing to its superior energy density, environmental benignity, and abundant availability. However, hydrogen storage limits its utilization of hydrogen energy. Various approaches for hydrogen storage have been explored, with solid-state hydrogen storage emerging as the predominant focus due to its high gravimetric hydrogen density, superior safety characteristics, and cost-effectiveness.

Magnesium hydride (MgH<sub>2</sub>), known for its high theoretical mass capacity (7.6 wt. %), high security, exceptional reversibility, cost-effectiveness, and non-toxicity, has emerged as a promising option for solid-state hydrogen storage mate-

Peer review under the responsibility of Chongqing University.

\* Corresponding authors.

E-mail addresses: [wangxinqiang@xatu.edu.cn](mailto:wangxinqiang@xatu.edu.cn) (X. Wang), [chenjian@xatu.edu.cn](mailto:chenjian@xatu.edu.cn) (J. Chen), [honggepan@zju.edu.cn](mailto:honggepan@zju.edu.cn), [\(H. Pan\).](mailto:hgpan@zju.edu.cn)

rials [11–14]. However, the thermodynamic stability and slow kinetic of the Mg/MgH<sub>2</sub> system require high temperatures, significantly hindering its practical application [15–19]. In recent years, ongoing advancements in the study of magnesium-based hydrogen storage materials have led to significant improvements in their hydrogen absorption and desorption performance [20–22]. So far, significant efforts have been dedicated to developing highly efficient catalysts and gaining a deeper understanding of their catalytic mechanisms, such as additive modification, [23] alloying, [24] and nano structuring [25–26].

Among these approaches, the incorporation of catalysts into MgH<sub>2</sub> to enhance hydrogen storage properties remains the most widely adopted due to its simplicity and effectiveness. Catalyst research to date has largely concentrated on a range of transition metals, such as nickel, cobalt, titanium, niobium, vanadium, molybdenum, and their compounds. Among these, Ti-based catalysts have demonstrated relatively high catalytic activity. For instance, Liang et al. [27] compared the catalytic performance of metals such as titanium, vanadium, manganese, nickel, and iron, and established the following sequence of catalytic activity for hydrogenation Mg-based hydrogen storage materials: Ti > V > Fe > Mn > Ni. Han et al. [28] employed first-principles calculations to show that Ti doping weakens the ionic interaction between Mg-H, which not only reduces the microscopic energy required for hydrogen atom removal but also lowers the macroscopic hydrogen desorption temperature. Although the catalytic performance of Ti has been extensively studied, single Ti-based catalysts still fail to meet the application demands of the Mg/MgH<sub>2</sub> system, necessitating further enhancement of their catalytic activity. Recent studies have demonstrated that the synergistic effects between two metal elements in bimetallic oxides can significantly improve the catalytic performance of various reactions. This synergy is also applicable to the catalysis of hydrogen storage materials based on magnesium materials and remains an active area of exploration. For example, Xian et al. [29] synthesized a two-dimensional Ti-Nb oxide nanosheet, TiNb<sub>2</sub>O<sub>7</sub>, which was incorporated into MgH<sub>2</sub> via ball milling. The observed reduction in the hydrogen desorption onset temperature of MgH<sub>2</sub> to 178 °C upon the incorporation of 3 wt. % catalysts can be ascribed to the combined catalytic effect between the two metal elements, resulting in a substantial 100 °C decrease compared to pure MgH<sub>2</sub>. Moreover, unique structures that may form during the catalyst preparation process have the potential to further enhance catalytic performance to some extent. Zhang et al. [4] employed a hydrothermal synthesis method to produce o-Nb<sub>2</sub>O<sub>5</sub>, resulting in a distinctive hollow morphology with porous structures. Their findings demonstrated that the incorporation of 7 wt. % o-Nb<sub>2</sub>O<sub>5</sub> notably lowered the initial dehydrogenation temperature of MgH<sub>2</sub> from 260 °C to a range between 250 °C and 195 °C. At 300 °C, the MgH<sub>2</sub> composite containing o-Nb<sub>2</sub>O<sub>5</sub> rapidly desorbed over 5.5 wt. % H<sub>2</sub>, and at 200 °C, it efficiently re-absorbed 5 wt. % of hydrogen within 30 s. The author proposed that the unique structural characteristics of the o-Nb<sub>2</sub>O<sub>5</sub> were in-

strumental in facilitating these enhanced hydrogenation and dehydrogenation behaviors. In addition, the hydrogen diffusion rate in magnesium-based alloys is markedly higher than that in pure MgH<sub>2</sub>. Consequently, the introduction of alloying elements to form multicomponent alloys or intermetallic compounds emerges as a potent strategy to improve both the kinetics and thermodynamics of the MgH<sub>2</sub> system. Chen et al. [8] introduced an efficient alloy catalyst for MgH<sub>2</sub> particles, comprising low-activity elements Mo and Ni (MoNi alloy). The *in-situ* generated MoNi and Mg<sub>2</sub>Ni nanoparticles tightly and uniformly encapsulate the MgH<sub>2</sub> core, establishing extensive interfaces that facilitate both hydrogen reaction sites and diffusion pathways. The MoNi-catalyzed Mg/MgH<sub>2</sub> system demonstrated a remarkable hydrogen absorption and release capacity of 6.7 wt. % at 300 °C, with hydrogen absorption occurring within 60 s and desorption within 10 min. This system exhibited exceptional cyclic stability and superior low-temperature hydrogen storage performance. These advancements provide significant impetus for further investigations into harnessing the synergistic interactions between metal elements to develop high-performance bimetallic catalysts [30–34].

Despite considerable advances in enhancing the hydrogen storage performance of MgH<sub>2</sub>, its properties still fall short of meeting the practical demands for solid-state hydrogen storage applications [18,35–36]. In this work, the innovative hollow microsphere structure of the Bi<sub>2</sub>Ti<sub>2</sub>O<sub>7</sub> catalyst is presented, which substantially enhances the hydrogen desorption and absorption processes of the Mg/MgH<sub>2</sub> system. The addition of only 10 wt. % Bi<sub>2</sub>Ti<sub>2</sub>O<sub>7</sub> hollow spheres reduces the MgH<sub>2</sub> desorption peak temperature to 245.6 °C, lowering the activation energy for dehydrogenation to 82.14 kJ·mol<sup>-1</sup>—an approximately 43 % reduction compared to pure MgH<sub>2</sub>. The investigation into the synergistic effects between elements reveals their significant impact on the hydrogen storage capabilities of the Mg/MgH<sub>2</sub> system. DFT calculations demonstrate that the alloying of Bi with Mg modulates the hydrogen binding free energy at the surface by altering the D-band electron density, thereby enabling the Bi<sub>2</sub>Mg<sub>3</sub> alloy to exhibit superior hydrogen adsorption and desorption properties. Additionally, through the hydrogen uptake and release processes, the *in-situ* synthesis of TiO<sub>2</sub> and other multivalent Ti species not only promotes extensive interactions between catalytic active sites and MgH<sub>2</sub> but also offers notable advantages in facilitating rapid electron transfer and the diffusion of hydrogen atoms or molecules. These attributes underscore the synergistic interaction between Bi and Ti, positioning Bi<sub>2</sub>Ti<sub>2</sub>O<sub>7</sub> as a promising catalyst for the Mg/MgH<sub>2</sub> system. This work provides a new highly effective bimetallic oxide as a catalyst for MgH<sub>2</sub>, and the proposed mechanism underlying its catalytic action.

## 2. Experimental and computational section

### 2.1. Synthesis of catalysts

**Fig. 1(a)** illustrates the synthesis of Bi<sub>2</sub>Ti<sub>2</sub>O<sub>7</sub> via the solvothermal method, along with a schematic representa-

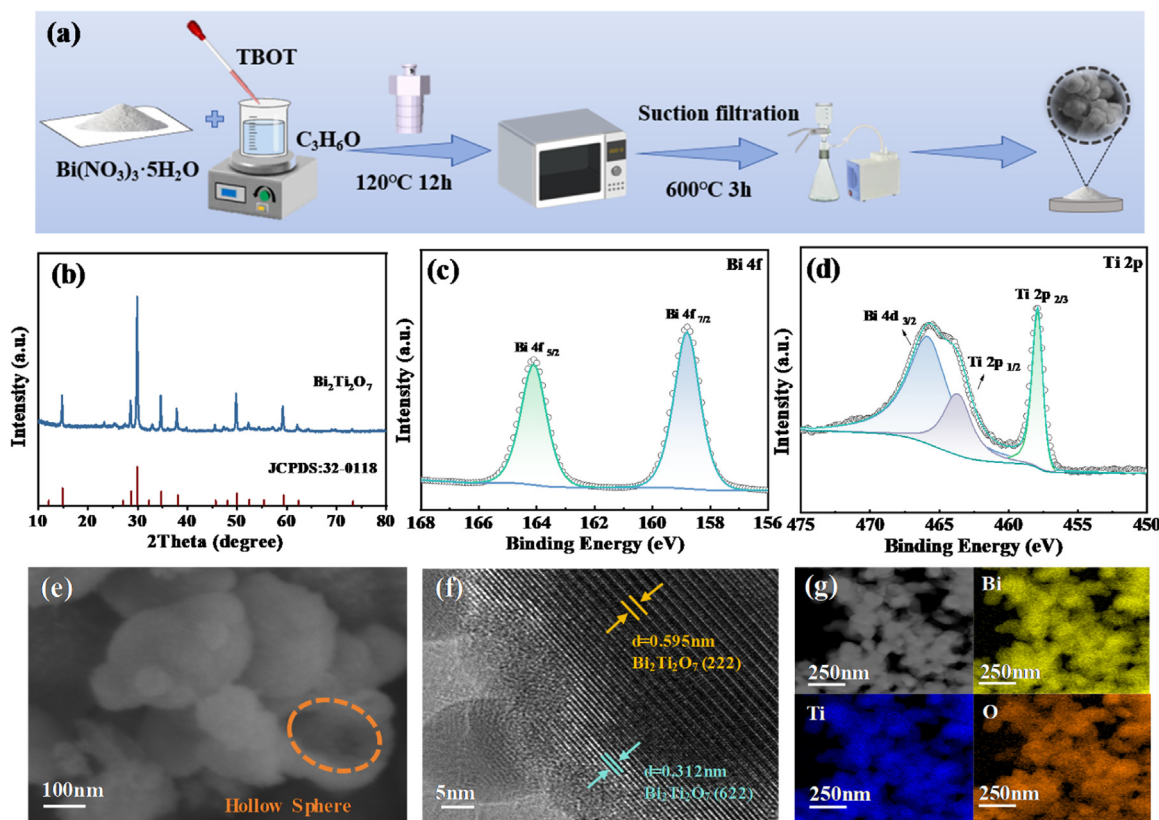


Fig. 1. (a) Schematic diagram of the preparation of Bi<sub>2</sub>Ti<sub>2</sub>O<sub>7</sub> particles; (b) XRD pattern of Bi<sub>2</sub>Ti<sub>2</sub>O<sub>7</sub> and (c, d) Bi 4f and Ti 2p XPS spectra for Bi<sub>2</sub>Ti<sub>2</sub>O<sub>7</sub> sample; the (e) SEM, (f) HRTEM, (g) corresponding EDS Mapping files of Bi<sub>2</sub>Ti<sub>2</sub>O<sub>7</sub> derivative.

tion of the preparation process. In the synthesis process, Mg (99.8 %, Macklin), Bi(NO<sub>3</sub>)<sub>3</sub>·5H<sub>2</sub>O (99.0 %, Macklin), Ti(OC<sub>4</sub>H<sub>9</sub>)<sub>4</sub> (99 %, Aladdin), and acetone (99 %, SCRC) were utilized. All chemicals were of analytical reagent grade and did not require further purification. Bi<sub>2</sub>Ti<sub>2</sub>O<sub>7</sub> microspheres were fabricated through a simple solvothermal method, employing bismuth nitrate (Bi(NO<sub>3</sub>)<sub>3</sub>·5H<sub>2</sub>O) and Ti(OC<sub>4</sub>H<sub>9</sub>)<sub>4</sub> as the precursor materials. Bi(NO<sub>3</sub>)<sub>3</sub>·5H<sub>2</sub>O (1 mmol) was dissolved in 20 mL of acetone solution, to which 1 mmol of TBOT was gradually added under vigorous stirring. The mixture was agitated for 2 h and treated with ultrasound for 15 min, after which the solution was transferred into a 50 mL Teflon-lined stainless autoclave and maintained at 120 °C for 12 h. The product was then filtered three times using anhydrous ethanol and deionized water, it was oven-dried at 60 °C for 2 h and then heated in air at 600 °C for 3 h. The calcined material was subsequently ground into a fine, uniform powder, yielding Bi<sub>2</sub>Ti<sub>2</sub>O<sub>7</sub> microspheres. For comparative analysis, Bi<sub>2</sub>O<sub>3</sub> and TiO<sub>2</sub> were synthesized by adding only Bi(NO<sub>3</sub>)<sub>3</sub>·5H<sub>2</sub>O or Ti(OC<sub>4</sub>H<sub>9</sub>)<sub>4</sub>, respectively, during the preparation process, employing the control-variable approach.

## 2.2. Preparation of MgH<sub>2</sub>-x wt. % Bi<sub>2</sub>Ti<sub>2</sub>O<sub>7</sub> (x = 6, 8, 10, 12) composites

MgH<sub>2</sub> was prepared independently by calcination in the laboratory. The MgH<sub>2</sub>-10 wt. % Bi<sub>2</sub>Ti<sub>2</sub>O<sub>7</sub> composite was fab-

ricated through high-energy ball milling. A mixture of 0.03 g of Bi<sub>2</sub>Ti<sub>2</sub>O<sub>7</sub> and 0.27 g of MgH<sub>2</sub> was placed in the milling jar, with a ball-to-material ratio of 60:1. The milling process was carried out within an argon-filled glove box. Milling was conducted at a rotational speed of 400 rpm for 6 h, employing a program that alternated between 24 min of operation and 6 min of rest. The resulting product was designated MgH<sub>2</sub>-10 wt. % Bi<sub>2</sub>Ti<sub>2</sub>O<sub>7</sub>. Similarly, MgH<sub>2</sub> composites with varying Bi<sub>2</sub>Ti<sub>2</sub>O<sub>7</sub> contents (x = 6, 8, 12 wt. %) were prepared under the same milling conditions for comparative analysis.

## 2.3. Characterization and hydrogen storage performance tests

The phase composition of the samples was assessed using an X-ray diffractometer (XRD, Empyrean from Malvern Panalytical) under an inert nitrogen atmosphere in an anaerobic glove box, employing a step size of  $2\theta = 0.02^\circ$  and a scan speed of 10°/min. The X-ray source used was Cu-K $\alpha$  radiation with a wavelength of 0.15406 Å. The microstructural characterization and lattice analysis of the samples were conducted using field emission scanning electron microscopy (FESEM, AMBER GMH from TESCAN) and transmission electron microscopy (TEM, JEM-F200 from Electron). Elemental distribution was mapped using TEM coupled with energy-dispersive spectroscopy (EDS, Super-X). Surface composition and elemental valence states were analyzed via X-

ray photoelectron spectroscopy (XPS, ESCALAB Xi+ from Thermo Scientific). Hydrogen storage performance was evaluated using a custom Sievert-type apparatus, following the volume method. In the temperature-programmed desorption test (TPD), the reactor was evacuated to 0.0001 MPa, and the sample was heated to 450 °C at a heating rate of 5 °C·min<sup>-1</sup>. During the non-isothermal hydrogenation process, the sample was exposed to 3 MPa H<sub>2</sub> and heating rate at 10 °C·min<sup>-1</sup> from room temperature to 300 °C. The hydrogen release peak temperature of various samples was measured using a Netzsch STA-449 differential scanning calorimeter (DSC). Additionally, the pressure-composition-temperature (PCT) curve of the dehydrogenation process was monitored using the Sievert-type apparatus, with dehydrogenation cycles performed at hydrogen pressures of 8 MPa and 0.0001 MPa, at 450 °C for desorption and 300 °C for absorption.

#### 2.4. Computational models and methods

All density functional theory (DFT) calculations were performed using the Vienna Ab-initio Simulation Package (VASP) [37–38]. The exchange-correlation interactions were modeled using the Perdew-Burke-Ernzerhof (PBE) functional within the framework of the generalized gradient approximation (GGA) method [39]. Core-valence interactions were treated using the projected augmented wave (PAW) method [40]. A plane-wave energy cutoff of 480 eV was applied, and a 3 × 3 × 1 Monkhorst-Pack k-point grid was used to sample the Brillouin zone. A vacuum space of 15 Å was introduced above the surfaces to eliminate periodic interactions. Structural optimization was performed using energy and force convergence criteria set to  $1.0 \times 10^{-4}$  eV and 0.02 eV Å<sup>-1</sup>, respectively.

### 3. Results and discussion

#### 3.1. Characterization of Bi<sub>2</sub>Ti<sub>2</sub>O<sub>7</sub> catalysts

The synthesized catalyst was thoroughly characterized, and phase analysis of Bi<sub>2</sub>Ti<sub>2</sub>O<sub>7</sub> was performed XRD, as shown in Fig. 1(b). In the XRD pattern of the composite material, the peaks corresponding to Bi<sub>2</sub>Ti<sub>2</sub>O<sub>7</sub> at various diffraction peaks were in excellent agreement with the standard XRD card (JCPDS: PDF#32–0118). Notable diffraction peaks appeared at 14.877°, 28.68°, and 29.96°, which are assigned to the (222), (622), and (444) planes, respectively. No additional diffraction peaks were observed and confirming that the synthesized material is predominantly composed of Bi<sub>2</sub>Ti<sub>2</sub>O<sub>7</sub> with high purity.

To further elucidate the elemental valence states, XPS was employed on the Bi<sub>2</sub>Ti<sub>2</sub>O<sub>7</sub> hollow spheres. As shown in Figs. 1(c) and (d), the XPS spectrum for Bi 4f (Fig. 1(c)) displays binding energy peaks at 158.8 eV and 164.2 eV, corresponding to the Bi 4f<sub>7/2</sub> and Bi 4f<sub>5/2</sub> peaks, respectively. These features are indicative of the presence of Bi<sup>3+</sup> in the octahedral structure of Bi<sub>2</sub>Ti<sub>2</sub>O<sub>7</sub>, consistent with the expected valence state. The Ti 2p XPS spectrum (Fig. 1(d))

shows Ti 2p<sub>3/2</sub> and Ti 2p<sub>1/2</sub> peaks at 463.7 eV and 457.6 eV, respectively, confirming that Ti is primarily in the Ti<sup>4+</sup> oxidation state on the sample surface. A broad peak near 465.0 eV, resulting from the overlap of Ti 2p<sub>1/2</sub> and Bi 4d<sub>3/2</sub> peaks, further supports this interpretation. These findings are in agreement with previous studies. Moreover, the full XPS spectrum of Bi<sub>2</sub>Ti<sub>2</sub>O<sub>7</sub>, together with the XPS spectra for the O and C elements, is presented in Supplementary Fig. S1. The C 1s spectrum facilitates the correction of peak positions, with a reference binding energy of 248.8 eV. The binding energy of O 1s, approximately 528.5 eV, further substantiates the oxidation state of the bimetallic oxide. SEM analysis of Bi<sub>2</sub>Ti<sub>2</sub>O<sub>7</sub> reveals a hollow microsphere structure, with the spheres adopting a clumped morphology (Fig. 1(e)). Building on previous studies [5], it is proposed that this hollow spherical architecture can substantially increase the material's specific surface area, thereby enhancing the number of active sites and, in turn, improving its catalytic efficiency. To investigate the crystalline structure, HRTEM was employed to measure lattice spacings in selected regions, as illustrated in Fig. 1(f). The interplanar distances of 0.312 nm and 0.595 nm correspond to the (622) and (222) planes of Bi<sub>2</sub>Ti<sub>2</sub>O<sub>7</sub>, respectively, which are in agreement with the XRD results. EDS mapping, presented in Fig. 1(g), reveals a uniform distribution of elements across the catalyst surface, with Bi, Ti, and O regions showing substantial overlap, thereby further validating the successful synthesis of Bi<sub>2</sub>Ti<sub>2</sub>O<sub>7</sub>.

For comparison purposes, XRD analysis was also performed on samples containing only Bi<sub>2</sub>O<sub>3</sub> and TiO<sub>2</sub>, as shown in Fig. S2. The diffraction peaks from the Bi-only sample were identified as Bi<sub>2</sub>O<sub>3</sub>, exhibiting a strong match with the standard XRD card (JCPDS no.32–0118). Similarly, the Ti-only sample displayed diffraction peaks consistent with TiO<sub>2</sub>, which also matched the standard XRD card (JCPDS no.32–0118). Fig. S3(a–d) illustrates the SEM images of the samples, offering a comprehensive comparison of their morphological characteristics. Bi<sub>2</sub>O<sub>3</sub> displays an irregular, rod-like structure, while TiO<sub>2</sub> is manifested as fine particulate aggregates. The distinctive morphology of the Bi<sub>2</sub>Ti<sub>2</sub>O<sub>7</sub> bimetallic oxide is likely to have played a significant role in enhancing its hydrogen storage performance.

#### 3.2. Characterization of MgH<sub>2</sub>–10 wt. % Bi<sub>2</sub>Ti<sub>2</sub>O<sub>7</sub> composites

Fig. 2(a) displays the XRD patterns of the Bi<sub>2</sub>Ti<sub>2</sub>O<sub>7</sub> catalyst before and after ball milling with MgH<sub>2</sub>. In the XRD pattern of the MgH<sub>2</sub>–10 wt. % Bi<sub>2</sub>Ti<sub>2</sub>O<sub>7</sub> composite post-ball milling, characteristic peaks of MgH<sub>2</sub> appear at 27.946°, 35.743°, 39.855°, and 54.616°, corresponding to the (110), (101), (200), and (211) planes, respectively. The diffraction peaks of Bi<sub>2</sub>Ti<sub>2</sub>O<sub>7</sub> in the composite are observed at 14.877°, 28.68°, and 29.96°, corresponding to the (222), (622), and (444) planes, respectively, confirming the thorough mixing of the two materials. Additionally, ball milling induces a partial reaction between Bi<sub>2</sub>Ti<sub>2</sub>O<sub>7</sub> and MgH<sub>2</sub>, resulting in

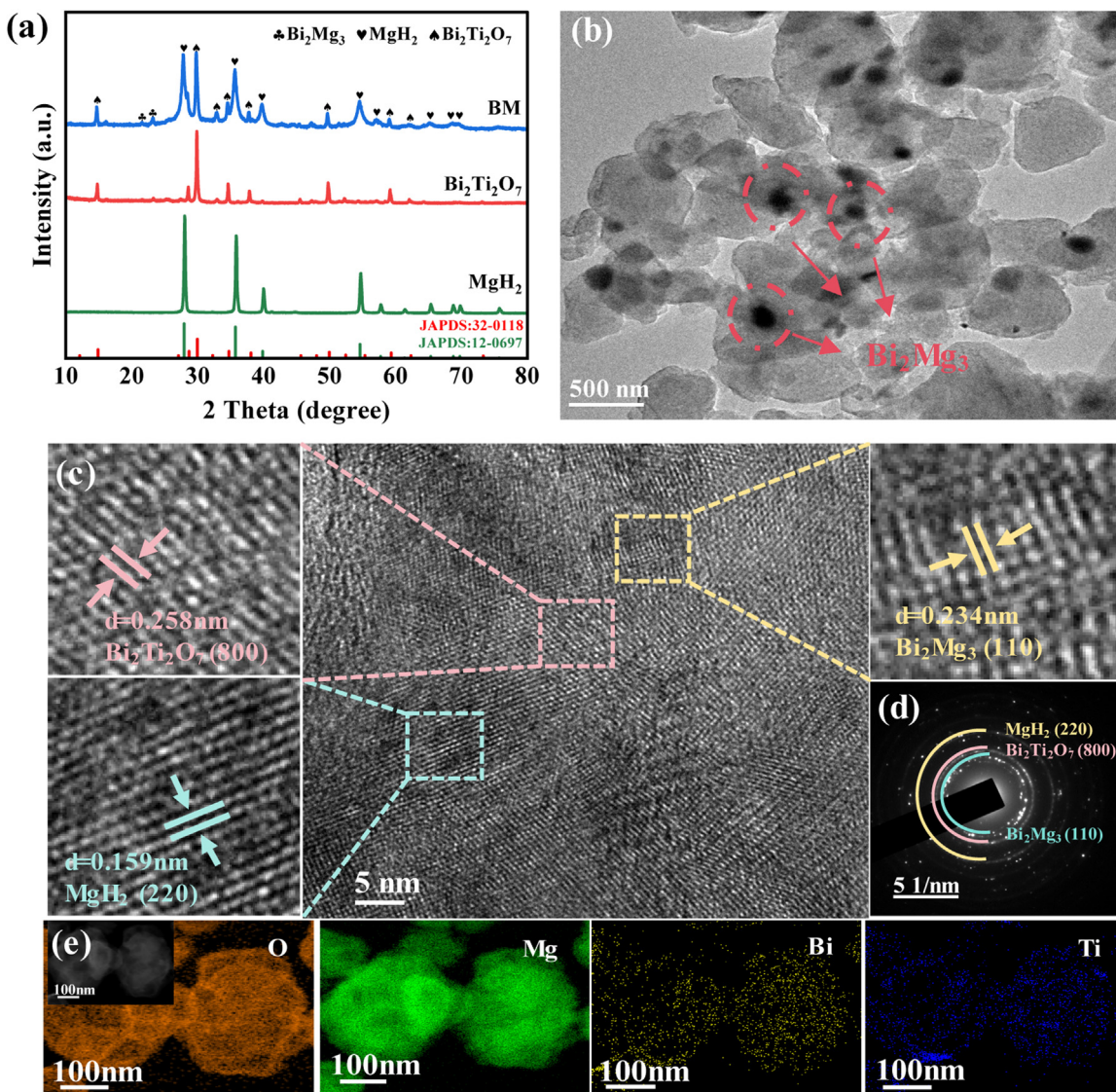


Fig. 2. (a) XRD pattern, (b) TEM, (c) HRTEM, (d) SAED pattern and (e) corresponding EDS elemental mapping files of as-prepared MgH<sub>2</sub>-10 wt % Bi<sub>2</sub>Ti<sub>2</sub>O<sub>7</sub>.

the formation of a small amount of Bi<sub>2</sub>Mg<sub>3</sub> alloy phase. Diffraction peaks observed at 23.966° and 25.063° correspond to the (002) and (101) planes of Bi<sub>2</sub>Mg<sub>3</sub>. Nonetheless, MgH<sub>2</sub> and Bi<sub>2</sub>Ti<sub>2</sub>O<sub>7</sub> remain the dominant phases. The milling process effectively reduces the particle size of both MgH<sub>2</sub> and Bi<sub>2</sub>Ti<sub>2</sub>O<sub>7</sub>. The TEM image in Fig. 2(b) reveals dark spots, which are tentatively identified as the Bi<sub>2</sub>Mg<sub>3</sub> alloy formed during milling. As shown in Fig. 2(c), lattice spacing measurements from selected regions yield values of  $d = 0.258$  nm, 0.159 nm, 0.234 nm, corresponding to the (800) plane of Bi<sub>2</sub>Ti<sub>2</sub>O<sub>7</sub>, the (220) plane of MgH<sub>2</sub>, and the (110) plane of Bi<sub>2</sub>Mg<sub>3</sub>, respectively. Furthermore, the SAED rings shown in Fig. 2(d) correspond to the (800) plane of Bi<sub>2</sub>Ti<sub>2</sub>O<sub>7</sub>, the (220) plane of MgH<sub>2</sub>, and the (110) plane of Bi<sub>2</sub>Mg<sub>3</sub>, further validating the presence of these three phases in the composite material. The increased number of crystal planes facilitates the destabilization of MgH<sub>2</sub>, enhancing its propensity for hydrogen release. Moreover, the distribution of

MgH<sub>2</sub>, Bi<sub>2</sub>Mg<sub>3</sub>, and Bi<sub>2</sub>Ti<sub>2</sub>O<sub>7</sub> is discernible through EDS elemental mapping (Fig. 2(e)). The overlapping regions of Mg and Bi enrichments correspond to Bi<sub>2</sub>Ti<sub>2</sub>O<sub>7</sub>, while the partial overlap of the Mg and Bi enrichments corresponds to the Bi<sub>2</sub>Mg<sub>3</sub> alloy. The EDS mapping confirms the uniform distribution of the elements within the composite material (Fig. 2(e)).

### 3.3. Hydrogen storage properties

To assess the synergistic effect of the Bi-Ti bimetallic catalyst, the dehydrogenation performance of the MgH<sub>2</sub>-10 wt % Bi<sub>2</sub>Ti<sub>2</sub>O<sub>7</sub> composite was compared to that of control samples. As shown in Fig. 3(a), under identical catalyst loading conditions, the MgH<sub>2</sub>-10 wt % Bi<sub>2</sub>Ti<sub>2</sub>O<sub>7</sub> composite exhibits the lowest hydrogen desorption temperature and the most rapid dehydrogenation kinetics. For the composite material doped with 10 wt % TiO<sub>2</sub>, the initial desorption temper-

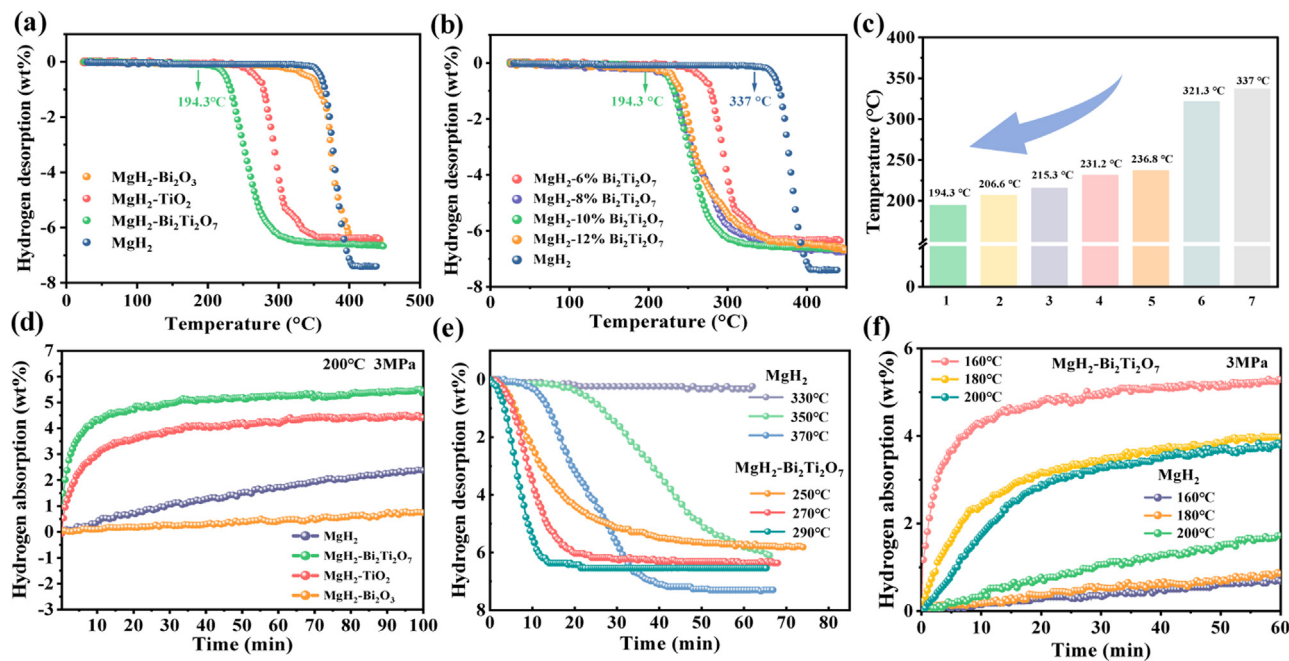


Fig. 3. (a) The rising temperature dehydrogenation curve for different catalysts and (b) MgH<sub>2</sub>-x wt.% Bi<sub>2</sub>Ti<sub>2</sub>O<sub>7</sub>; (c) the histograms of dehydrogenation activation energy of different composites, composites 1 to 7 are MgH<sub>2</sub>-10 wt.% Bi<sub>2</sub>Ti<sub>2</sub>O<sub>7</sub>, MgH<sub>2</sub>-8 wt.% Bi<sub>2</sub>Ti<sub>2</sub>O<sub>7</sub>, MgH<sub>2</sub>-12 wt.% Bi<sub>2</sub>Ti<sub>2</sub>O<sub>7</sub>, MgH<sub>2</sub>-10 wt.% TiO<sub>2</sub>, MgH<sub>2</sub>-6 wt.% Bi<sub>2</sub>Ti<sub>2</sub>O<sub>7</sub>, MgH<sub>2</sub>-10 wt.% Bi<sub>2</sub>O<sub>3</sub> and MgH<sub>2</sub>; (d) isothermal dehydrogenation curve prepared at 300 °C of different catalysts; (e) isothermal dehydrogenation (f) absorption curves at different temperatures for MgH<sub>2</sub> and MgH<sub>2</sub>-10 wt.% Bi<sub>2</sub>Ti<sub>2</sub>O<sub>7</sub>.

ature is reduced to 220 °C, representing a notable improvement over pure MgH<sub>2</sub>; however, it remains higher than that of the MgH<sub>2</sub>-10 wt.% Bi<sub>2</sub>Ti<sub>2</sub>O<sub>7</sub> composite. Surprisingly, the incorporation of Bi<sub>2</sub>O<sub>3</sub> did not lead to a significant enhancement in the dehydrogenation performance of MgH<sub>2</sub>. While a modest reduction in the initial desorption temperature was observed, decreasing from 337 °C to 321.3 °C, the peak desorption temperature remained similar to that of pure MgH<sub>2</sub>. Furthermore, the overall hydrogen release was even lower, dropping from approximately 7.5 wt.% to 6.3 wt.%, thus underscoring the absence of any appreciable catalytic activity. To elucidate the catalytic role of Ti species, XRD characterization was performed on both MgH<sub>2</sub>-Bi<sub>2</sub>Ti<sub>2</sub>O<sub>7</sub> and MgH<sub>2</sub>-Bi<sub>2</sub>O<sub>3</sub> composites in their as-milled state and after initial dehydrogenation. Fig. S4(a) reveals that no Bi<sub>2</sub>Mg<sub>3</sub> alloy phase formed in the MgH<sub>2</sub>-Bi<sub>2</sub>O<sub>3</sub> composite after ball-milling, resulting in a lack of catalytic active sites during initial dehydrogenation. Fig. S4(b) shows that there is a distinct Bi<sub>2</sub>Mg<sub>3</sub> alloy phase in the composite material after dehydrogenation. From this, it can be inferred that the Bi<sub>2</sub>Mg<sub>3</sub> alloy phase is more likely to form under high-temperature conditions, and the presence of Ti<sup>4+</sup> in Bi<sub>2</sub>Ti<sub>2</sub>O<sub>7</sub> accelerates this process. These findings underscore the indispensable role of multivalent metal oxides in the catalytic modification of MgH<sub>2</sub>, particularly highlighting the advantages of Ti-containing catalysts in maintaining reversible redox cycles and stable catalytic interfaces.

To further explore the catalytic role of the hollow-sphere Bi<sub>2</sub>Ti<sub>2</sub>O<sub>7</sub> bimetallic oxide in improving the hydrogen storage performance of MgH<sub>2</sub>, the dehydrogenation performance

of ball-milled composites containing varying amounts of Bi<sub>2</sub>Ti<sub>2</sub>O<sub>7</sub> (MgH<sub>2</sub>-x wt.% Bi<sub>2</sub>Ti<sub>2</sub>O<sub>7</sub>) was investigated, as shown in Fig. 3(b). Pure MgH<sub>2</sub> exhibited a high initial desorption temperature of 335 °C. The comparison of dehydrogenation performances reveals that the MgH<sub>2</sub>-10 wt.% Bi<sub>2</sub>Ti<sub>2</sub>O<sub>7</sub> composite demonstrates the most remarkable results, exhibiting an initial desorption temperature of 194.3 °C and a final hydrogen desorption of 6.59 wt.%. The difference in initial desorption temperature between target and control samples is highlighted in Fig. 3(c). Furthermore, as shown in Fig. S5, compared to previously reported catalytic systems, our catalyst showed excellent performance at initial desorption temperatures, maintaining a high amount of dehydrogenation even at relatively low starting temperatures. Comprehensive comparative data of representative samples are provided in Table S1 of the Supporting Information [4,11,29,41–45]. To further elucidate the differences in hydrogen storage capabilities, isothermal hydrogen absorption tests were conducted at 200 °C and 3 MPa, as depicted in Fig. 3(d). Under the same conditions, the MgH<sub>2</sub>-10 wt.% Bi<sub>2</sub>Ti<sub>2</sub>O<sub>7</sub> composite reaches a hydrogen absorption of 5.14 wt.% within approximately 30 min, whereas the MgH<sub>2</sub>-10 wt.% TiO<sub>2</sub> composite absorbs only 3.95 wt.% H<sub>2</sub>. Interestingly, the MgH<sub>2</sub>-10 wt.% Bi<sub>2</sub>O<sub>3</sub> composite even shows poorer hydrogen absorption than pure MgH<sub>2</sub>, suggesting that this material is almost non-recyclable. By observing Fig. S4(b), it was found that Bi<sub>2</sub>O<sub>3</sub> was almost completely consumed after dehydrogenation, lacking a reversible electron transfer pathway. Therefore, Bi<sub>2</sub>O<sub>3</sub> can only be irreversibly reduced to Bi<sup>0</sup> (Bi<sup>3+</sup>→Bi<sup>0</sup>), which hinders the continuous supply of active sites in subsequent cycles and

leads to a poor hydrogen absorption effect. From the comparative hydrogen absorption and desorption data, it is evident that the synergistic interaction between the Bi and Ti metal elements within the catalyst significantly enhances the kinetic properties of MgH<sub>2</sub> [46].

Subsequent measurements were conducted on the isothermal hydrogen absorption and desorption curves of pure MgH<sub>2</sub> and MgH<sub>2</sub>-10 wt. % Bi<sub>2</sub>Ti<sub>2</sub>O<sub>7</sub> composites across a range of temperatures. As illustrated in Fig. 3(e), the MgH<sub>2</sub>-10 wt. % Bi<sub>2</sub>Ti<sub>2</sub>O<sub>7</sub> composite achieved a hydrogen desorption capacity of 6.3 wt. % within 15 min at 290 °C, whereas pure MgH<sub>2</sub> showed no detectable desorption initiation under identical conditions. Even at an elevated temperature of 350 °C, pure MgH<sub>2</sub> released only 1.63 wt. % hydrogen after 20 min. These results demonstrate that Bi<sub>2</sub>Ti<sub>2</sub>O<sub>7</sub> incorporation significantly enhances the dehydrogenation performance of MgH<sub>2</sub>, enabling higher hydrogen release yields at substantially reduced temperatures. Fig. 3(f) presents the isothermal hydrogen absorption data for both pure MgH<sub>2</sub> and MgH<sub>2</sub>-10 wt. % Bi<sub>2</sub>Ti<sub>2</sub>O<sub>7</sub> composites under 3 MPa pressure at various temperatures. At 200 °C, the fully dehydrogenated MgH<sub>2</sub>-10 wt. % Bi<sub>2</sub>Ti<sub>2</sub>O<sub>7</sub> composite absorbed 5.29 wt. % H<sub>2</sub> within 60 min, while pure MgH<sub>2</sub> achieved merely 1.66 wt. % H<sub>2</sub> absorption under identical conditions. These findings conclusively indicate that undoped MgH<sub>2</sub> requires significantly higher operational temperatures to attain hydrogen sorption performance comparable to the Bi<sub>2</sub>Ti<sub>2</sub>O<sub>7</sub>-modified material. In summary, the catalytic doping strategy developed in this study substantially enhances both hydrogen absorption and release properties of MgH<sub>2</sub>, presenting a promising pathway for advancing magnesium-based hydrogen storage materials.

### 3.4. Dehydrogenation kinetics and thermodynamics

The thermodynamic and kinetic impacts of the Bi<sub>2</sub>Ti<sub>2</sub>O<sub>7</sub> catalyst on the dehydrogenation behavior of MgH<sub>2</sub> were further examined through DSC, and the Kissinger method [47]. Figs. 4(a-b) present the DSC curves for both pure MgH<sub>2</sub> and the MgH<sub>2</sub>-10 wt. % Bi<sub>2</sub>Ti<sub>2</sub>O<sub>7</sub> composite, recorded at heating rates of 3 °C·min<sup>-1</sup>, 5 °C·min<sup>-1</sup>, 7 °C·min<sup>-1</sup> and 10 °C·min<sup>-1</sup>. The DSC curve of pure MgH<sub>2</sub> at a heating rate of 3 °C·min<sup>-1</sup> shows a dehydrogenation peak at approximately 339 °C. In contrast, when Bi<sub>2</sub>Ti<sub>2</sub>O<sub>7</sub> is incorporated, the dehydrogenation peak for the MgH<sub>2</sub>-10 wt. % Bi<sub>2</sub>Ti<sub>2</sub>O<sub>7</sub> composite shifts to a significantly lower temperature. Specifically, the dehydrogenation peak temperature for this composite drops to 245.6 °C, marking a reduction of 93.4 °C compared to pure MgH<sub>2</sub>. This marked decrease in the dehydrogenation peak temperature underscores the enhanced catalytic activity of Bi<sub>2</sub>Ti<sub>2</sub>O<sub>7</sub>. To further probe the dehydrogenation kinetics of the composite material, the activation energy ( $E_a$ ) for hydrogen desorption was calculated using the Kissinger method (Equation (1)), derived from the DSC data:

$$\ln \left( \frac{\beta}{T_p^2} \right) = -\frac{E_a}{RT_p} + \ln (AR/E_a) \quad (1)$$

The parameters  $\beta$ ,  $T_p$ ,  $A$ , and  $R$  represent the heating rate, the absolute temperature at the peak desorption rate, the factor before the exponential term, and the gas constant, respectively. The value of  $T_p$  is derived from the DSC curves shown in Fig. 4(c). The activation energy ( $E_a$ ) of the samples was determined by fitting the data presented in Figs. 4(a-b). As shown in Fig. 4(c), in comparison to the high  $E_a$  of pure MgH<sub>2</sub> (approximately 141.67 kJ·mol<sup>-1</sup>), the  $E_a$  for the MgH<sub>2</sub>-10 wt. % Bi<sub>2</sub>Ti<sub>2</sub>O<sub>7</sub> composite is notably reduced to 82.14 kJ·mol<sup>-1</sup>. This substantial reduction directly attests to the ability of the Bi<sub>2</sub>Ti<sub>2</sub>O<sub>7</sub> catalyst to lower the dehydrogenation kinetic barrier of MgH<sub>2</sub>. Furthermore, as shown in Fig. S6 and Table S2, MgH<sub>2</sub>-10 wt. % Bi<sub>2</sub>Ti<sub>2</sub>O<sub>7</sub> composites have a relatively low  $E_a$  compared to many other hydrogen storage materials of the same type [11,29,42,48-49].

In addition, PCT measurements were carried out to further explore the thermodynamic properties of the MgH<sub>2</sub>-10 wt. % Bi<sub>2</sub>Ti<sub>2</sub>O<sub>7</sub> composite, as illustrated in Figs. 4(d-e). During the dehydrogenation process, each PCT curve shows a single flat plateau at a given temperature, corresponding to the decomposition of MgH<sub>2</sub> into Mg and H<sub>2</sub>. Based on PCT data, the decomposition enthalpy ( $\Delta H$ ) was estimated using the Van't Hoff equation [50] (Eq. (2)):

$$\ln P = \frac{\Delta H}{RT} - \Delta S/R \quad (2)$$

The parameters  $P$ ,  $\Delta S$ ,  $R$ , and  $T$  correspond to pressure, decomposition entropy, the ideal gas constant, and temperature, respectively. The Van't Hoff plot derived from these measurements is shown in Fig. 4(f). These PCT curves are employed to assess the effect of the Bi<sub>2</sub>Ti<sub>2</sub>O<sub>7</sub> catalyst on the thermodynamic behavior of MgH<sub>2</sub>. The curves for the MgH<sub>2</sub>-10 wt. % Bi<sub>2</sub>Ti<sub>2</sub>O<sub>7</sub> composite at temperatures of 320, 340, and 360 °C are presented in Fig. 4(e). At the four temperatures, the equilibrium pressure of hydrogen absorption is 0.251, 0.381, 0.702 and 0.989 MPa, respectively. Based on PCT data and using Van't Hoff equation (calculation of decomposition heat  $\Delta H$ ), the fitting Fig. 4(f) obtained shows that the  $\Delta H$  of the dehydrogenation process of MgH<sub>2</sub>-10 wt. % Bi<sub>2</sub>Ti<sub>2</sub>O<sub>7</sub> is 80.97 kJ·mol<sup>-1</sup>, which is close to the 81.72 kJ·mol<sup>-1</sup> of the measured MgH<sub>2</sub>. This finding suggests that the enthalpy change of the MgH<sub>2</sub>-10 wt. % Bi<sub>2</sub>Ti<sub>2</sub>O<sub>7</sub> composite material remains largely unchanged, in line with previous reports that the addition of catalysts does not significantly affect the thermodynamic properties of MgH<sub>2</sub> [51-52].

### 3.5. Cycling hydrogen storage properties

To assess the cycling stability of the hydrogen storage material, the dehydrogenation performance of the MgH<sub>2</sub>-10 wt. % Bi<sub>2</sub>Ti<sub>2</sub>O<sub>7</sub> composite was evaluated at 300 °C over multiple cycles, as depicted in Fig. 5(a). The results demonstrate the composite's excellent cycling stability. During the initial desorption cycle, a hydrogen release of 6.59 wt. % was achieved. However, subsequent cycles revealed a noticeable decline in hydrogen desorption, with the release decreasing to 5.3 wt. % after the fourth cycle. Notably, by the fiftieth cy-

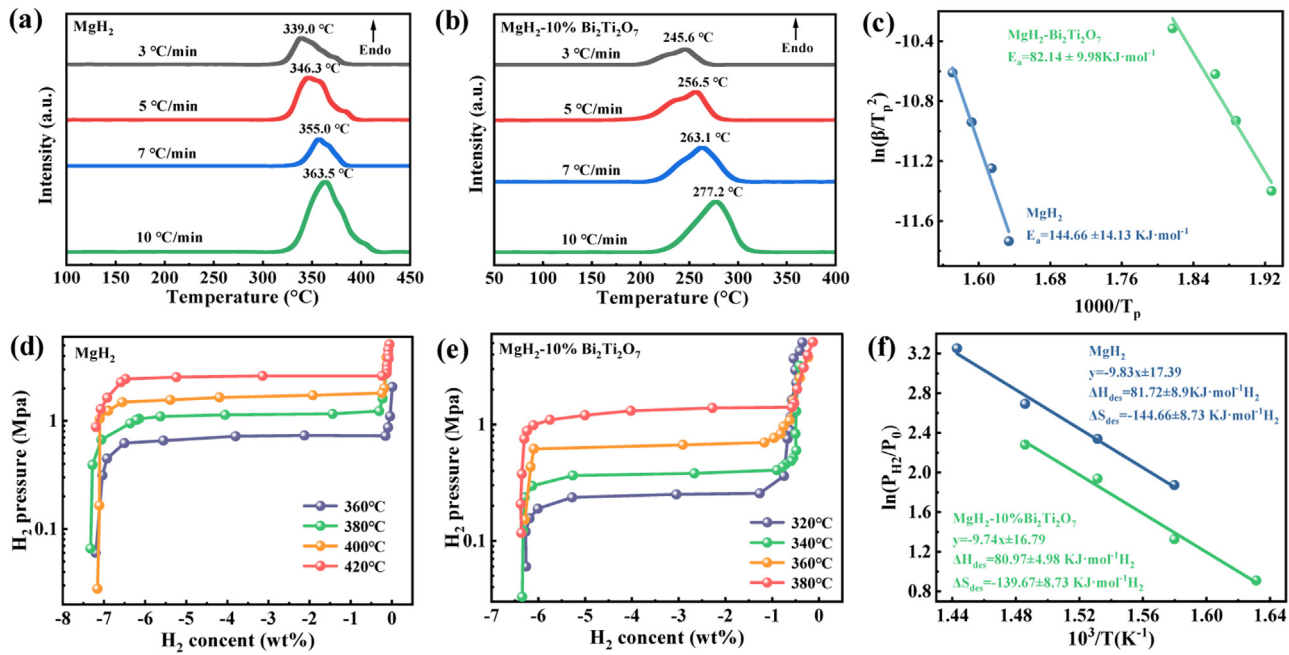


Fig. 4. (a-c) DSC curves and corresponding Kissinger plots of MgH<sub>2</sub> and MgH<sub>2</sub>-10 wt. % Bi<sub>2</sub>Ti<sub>2</sub>O<sub>7</sub>; (d-f) PCT curves and corresponding van't Hoff plots of MgH<sub>2</sub> and MgH<sub>2</sub>-10 wt. % Bi<sub>2</sub>Ti<sub>2</sub>O<sub>7</sub>.

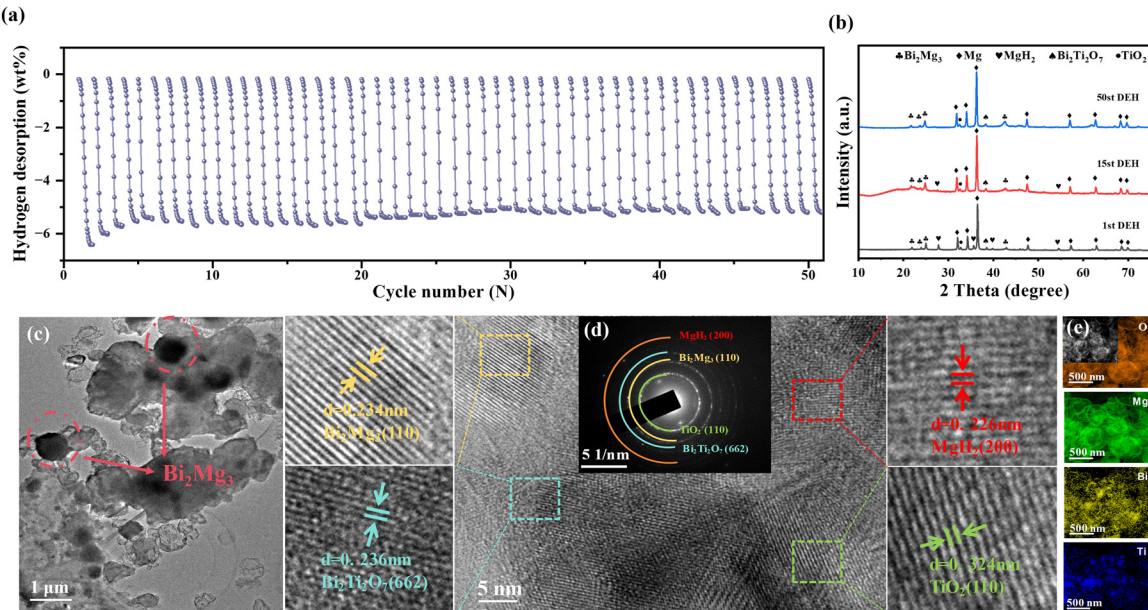


Fig. 5. (a) Cycling profile of the MgH<sub>2</sub>-10 wt. % Bi<sub>2</sub>Ti<sub>2</sub>O<sub>7</sub>; (b) XRD patterns of MgH<sub>2</sub>-10 wt. % Bi<sub>2</sub>Ti<sub>2</sub>O<sub>7</sub> dehydrogenated after 1 cycle, 15 cycles, and 50 cycles; (c) TEM, (d) HRTEM and its SAED pattern; (e) corresponding EDS elemental mapping files of MgH<sub>2</sub>-10 wt. % Bi<sub>2</sub>Ti<sub>2</sub>O<sub>7</sub> dehydrogenated after 15 cycles.

cle, hydrogen desorption stabilized at 5.2 wt. %, maintaining 98.1% of its initial capacity from the fifth to the fiftieth cycle. In practical applications, maintaining superior hydrogen storage performance over repeated cycles is essential for the advancement of magnesium-based hydrogen storage materials.

To explore the underlying reasons for the observed decrease in hydrogen desorption, comprehensive characteriza-

tion analyses were performed on the material before and after hydrogen absorption/desorption as well as during cycling. XRD was conducted on the material after the first, fifteenth, and fiftieth desorption cycles, as shown in Fig. 5(b). The results reveal that, after 15 and 50 cycles, the material's composition remained largely unchanged compared to the first desorption cycle. Mg still predominated, but a small amount of MgH<sub>2</sub> remained, as evidenced by a diffraction peak at

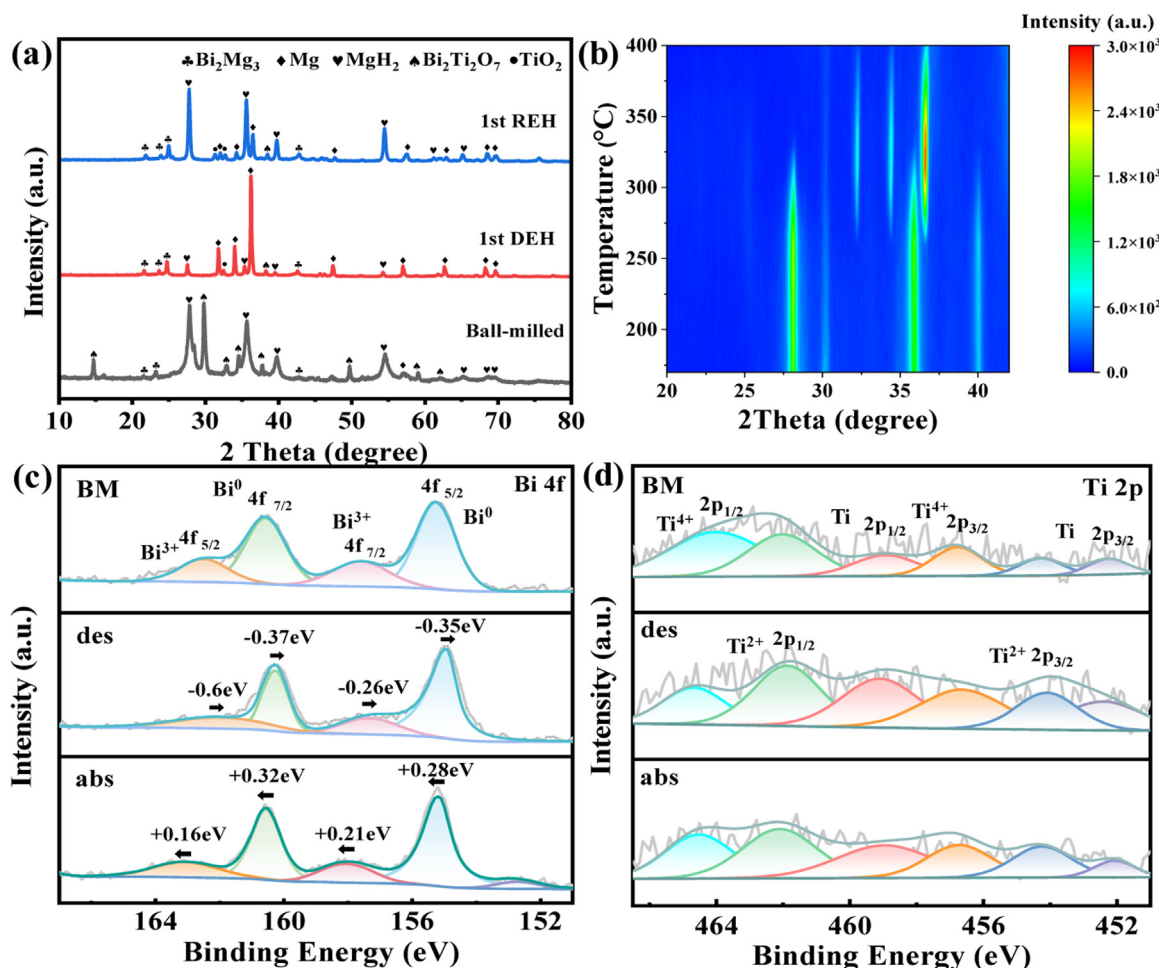


Fig. 6. (a) XRD patterns of MgH<sub>2</sub>-10 wt. % Bi<sub>2</sub>Ti<sub>2</sub>O<sub>7</sub> after ball milling, hydrogen absorption and desorption; (b) *in-situ* XRD patterns of MgH<sub>2</sub>-10 wt. % Bi<sub>2</sub>Ti<sub>2</sub>O<sub>7</sub> with temperature variation; (c-d) high resolution XPS spectra of Bi 4f, and Ti 2p of MgH<sub>2</sub>-10 wt. % Bi<sub>2</sub>Ti<sub>2</sub>O<sub>7</sub> composites after ball milling, hydrogen absorption and desorption.

39.855°, corresponding to the (200) plane. Incomplete dehydrogenation was identified as a contributing factor to the decrease in cycling capacity. Fig. S7 presents the XRD patterns of the composite after ball milling, as well as after the 1st, 15th, and 50th hydrogen absorption cycles. The analysis reveals that the diffraction peaks corresponding to the Bi<sub>2</sub>Mg<sub>3</sub> alloy phase and metallic Mg are significantly intensified compared to those after the initial hydrogen absorption. The enhanced peaks of the Bi<sub>2</sub>Mg<sub>3</sub> phase suggest that this alloy becomes more stable during repeated hydrogenation/dehydrogenation cycles due to the optimized interfacial structure. The increased intensity of the Mg peaks indicates that the dehydrogenation of MgH<sub>2</sub> proceeds more completely, with the released Mg not being fully rehydrogenated. These findings demonstrate that the composite develops a stable catalytic-alloy synergistic mechanism during cycling. In the TEM characterization of Fig. 5(c), the dark spots consistent with that in Fig. 2(b) can be clearly observed, corresponding to the stable Bi<sub>2</sub>Mg<sub>3</sub> alloy phase in the process of hydrogen absorption and desorption. The measurement results of lattice spacing in selected areas are shown in Fig. 5(d). The part of

crystal plane spacing of 0.234 nm corresponds to the (110) crystal face of Bi<sub>2</sub>Mg<sub>3</sub>, and the part of crystal plane spacing of 0.324 nm corresponds to the (110) crystal face of TiO<sub>2</sub>, and the measurement results are also reflected in the SAED diffraction ring. The above characterization analysis confirms the accuracy of XRD. In addition, EDS observations of the material in Fig. 5(e) show that Mg elements partially overlap with Bi elements, which also confirms the above speculation. Additionally, SEM images of the composite material after ball milling, dehydrogenation, and 15 cycles are shown in Fig. S8. SEM observations revealed significant particle agglomeration after hydrogen absorption, which contributed to a reduction in desorbed hydrogen during the second cycle. However, after ten cycles, the particles were observed to disperse into finer particles, which likely accounts for the stabilization of desorption capacity from the sixth cycle onward.

### 3.6. Analysis of catalytic mechanisms

Fig. 6(a) displays the XRD patterns of the composite material following ball milling and subsequent hydrogen absor-

tion/desorption cycles. The results demonstrate that, after dehydrogenation, the MgH<sub>2</sub> phase largely vanishes, with Mg emerging as the predominant phase. Characteristic diffraction peaks at 32.193°, 34.398°, and 36.619° correspond to the (100), (002), and (101) planes, respectively. The Bi<sub>2</sub>Mg<sub>3</sub> alloy phase becomes more discernible, while a small amount of TiO<sub>2</sub> is also detected, with a peak at 39.187° corresponding to the (200) plane. Due to the relatively low catalyst content, the TiO<sub>2</sub> peaks are subtle. After hydrogen reabsorption, the Mg characteristic peaks remain partially visible at 36.619° (the (101) plane), indicating that the hydrogenation of the Mg phase is incomplete. The presence of the Bi<sub>2</sub>Mg<sub>3</sub> alloy phase remains evident, confirming that it stabilizes during the hydrogen absorption and desorption cycles, contributing catalytically to the process. Further *in-situ* XRD measurements were performed during the heating desorption process within the temperature range of 150 °C to 400 °C, as shown in Fig. 6(b). At temperatures of 250 °C and 300 °C, the Mg diffraction peaks emerge, while the MgH<sub>2</sub> peaks persist, suggesting partial decomposition of MgH<sub>2</sub>. At 350 °C, only Mg peaks are observed, indicating nearly complete decomposition of MgH<sub>2</sub>. Additionally, weak peaks associated with the MgO phase appear alongside the main Mg peaks, likely due to the slight oxidation of the material, resulting in the formation of a MgO layer on the surface of the Mg particles.

In addition, XPS analysis was performed to gain deeper insights into the changes in the valence states of Bi and Ti during the ball milling, dehydrogenation, and hydrogenation processes. Figs. 6(c-d) depict the evolution of the valence states of these elements. The Bi 4f XPS spectrum of the ball-milled product was deconvoluted into two pairs of XPS peaks corresponding to the 4f<sub>5/2</sub> and 4f<sub>7/2</sub> spin-orbit components, revealing the presence of Bi<sup>3+</sup> (162.34 eV/157.43 eV) and Bi<sup>0</sup> (160.56 eV/155.24 eV). This confirms that, during ball milling, a portion of the Bi was reduced from the Bi<sup>3+</sup> state to the metallic Bi<sup>0</sup> state. During dehydrogenation, the catalyst continued to undergo reduction, and Bi reacted with Mg to form the Bi<sub>2</sub>Mg<sub>3</sub> alloy. Additionally, the XPS spectra collected after hydrogen absorption and desorption cycles exhibited no significant changes, indicating that both the oxidation and metallic states of Bi remained stable throughout the hydrogenation and dehydrogenation processes. During ball milling, the MgH<sub>2</sub>-10 wt.% Bi<sub>2</sub>Ti<sub>2</sub>O<sub>7</sub> composite interacted with MgH<sub>2</sub> to form TiO<sub>2</sub>, which persisted throughout the process. Reduction reactions also occurred, resulting in the formation of small amounts of Ti<sup>3+</sup> and Ti<sup>0</sup>, which can serve as an electron transfer mediator that accelerates the dehydrogenation reaction, thereby promoting the formation of the Bi<sub>2</sub>Mg<sub>3</sub> alloy phase. Although the Ti content was relatively low, preventing the appearance of distinct Ti peaks in the XRD data, these changes were identified by the XPS spectra. The involvement of multivalent Ti in the reaction aided electron transfer between Mg<sup>2+</sup> and H<sup>-</sup>, thus promoting the dehydrogenation [50]. In addition, As shown in Fig. S9(b), after hydrogen absorption, the binding energy of lattice oxygen in the composite recovers to a level close to that of the ball-milled state, while the surface hydroxyl binding energy

slightly decreases. Concurrently, new surface-adsorbed oxygen peaks emerge, accompanied by the formation of oxygen vacancies. During catalysis, these oxygen vacancies function as preferential adsorption and reaction sites. By providing specific chemical environments, they facilitate reaction progression. Moreover, the oxygen vacancies enhance the charge transfer of electrons or holes, thereby altering the chemical reaction rates and influencing the kinetic processes of the reaction.

To further explore the catalytic role of Bi<sub>2</sub>Ti<sub>2</sub>O<sub>7</sub> in enhancing the hydrogen storage capacity of MgH<sub>2</sub>, DFT calculations were performed to elucidate the underlying mechanisms. The initial computational model, as previously described, underwent structural optimization to achieve a more stable configuration. The (444) crystal plane of Bi<sub>2</sub>Ti<sub>2</sub>O<sub>7</sub> was selected for analysis, as it is the most likely to be exposed during the process. Charge transfer between MgH<sub>2</sub> and Bi<sub>2</sub>Ti<sub>2</sub>O<sub>7</sub> was investigated using electron density difference (EDD) and Bader charge distribution analyses (Fig. 7(a)), Fig. S10 shows other supported views. The EDD diagram in Fig. 7(a) indicates that MgH<sub>2</sub> adsorbs onto the O atom, and charge transfer occurs between the MgH<sub>2</sub> and Bi<sub>2</sub>Ti<sub>2</sub>O<sub>7</sub> interface, making the Mg-H bond unstable. This catalyzes the decomposition of MgH<sub>2</sub> and promotes the formation of the Bi<sub>2</sub>Mg<sub>3</sub> alloy. Meanwhile, the DOS result in Fig. 7(e) shows a hybridization between the Bi p orbitals and the Mg p orbitals, indicating that the Bi<sub>2</sub>Mg<sub>3</sub> alloy phase can be easily generated after the interaction with Bi<sub>2</sub>Ti<sub>2</sub>O<sub>7</sub> and MgH<sub>2</sub>, further verifying the above conclusion. Furthermore, the hybridization was found between Ti 3d and H 1s in the DOS diagram, indicating a strong interaction between Ti and H, which led to an increase in the polarity of the Mg-H bond and an elongation of the bond length, thereby reducing the kinetic barrier of hydrogen release.

In order to deeply study the mechanism of action of Bi<sub>2</sub>Ti<sub>2</sub>O<sub>7</sub>, Bi<sub>2</sub>Mg<sub>3</sub> was incorporated into the computational model and discussed and analyzed together with Bi<sub>2</sub>Ti<sub>2</sub>O<sub>7</sub> and the comparison sample TiO<sub>2</sub>. The results in Fig. 7(b) and Fig. S11 demonstrate that the Mg-H bond lengths in MgH<sub>2</sub>-Bi<sub>2</sub>Ti<sub>2</sub>O<sub>7</sub>, MgH<sub>2</sub>-Bi<sub>2</sub>Mg<sub>3</sub>, and MgH<sub>2</sub>-TiO<sub>2</sub> systems measure 1.83 Å, 1.792 Å, and 1.70 Å, respectively. Among them, the Mg-H bond under the influence of Bi<sub>2</sub>Ti<sub>2</sub>O<sub>7</sub> and Bi<sub>2</sub>Mg<sub>3</sub> was significantly longer than the 1.71 Å bond length of the original MgH<sub>2</sub> [53]. This elongation demonstrates that the Bi<sub>2</sub>Ti<sub>2</sub>O<sub>7</sub> and Bi<sub>2</sub>Mg<sub>3</sub> alloy can weaken the Mg-H bond strength, facilitating bond cleavage and consequently lowering the dehydrogenation temperature of MgH<sub>2</sub> [54]. Fig. 7(c) shows the negative adsorption energies of the three systems, confirming the exothermic H<sub>2</sub> adsorption process. The lower adsorption energy is associated with higher system stability, indicating that both Bi<sub>2</sub>Ti<sub>2</sub>O<sub>7</sub> and Bi<sub>2</sub>Mg<sub>3</sub> have good adsorption capacities. Compared to the reference 1.21 eV dissociation barrier on Mg(0001) surfaces (the rate-limiting step in hydrogenation) [55], Fig. 7(d) shows that Bi<sub>2</sub>Ti<sub>2</sub>O<sub>7</sub> and its derived Bi<sub>2</sub>Mg<sub>3</sub> phase significantly reduce this barrier to 0.33 eV and 0.47 eV respectively, while TiO<sub>2</sub> only reaches 1.14 eV. This indicates that Bi<sub>2</sub>Ti<sub>2</sub>O<sub>7</sub> and Bi<sub>2</sub>Mg<sub>3</sub> promote the dissociation of H<sub>2</sub>, highlighting their special catalytic ac-

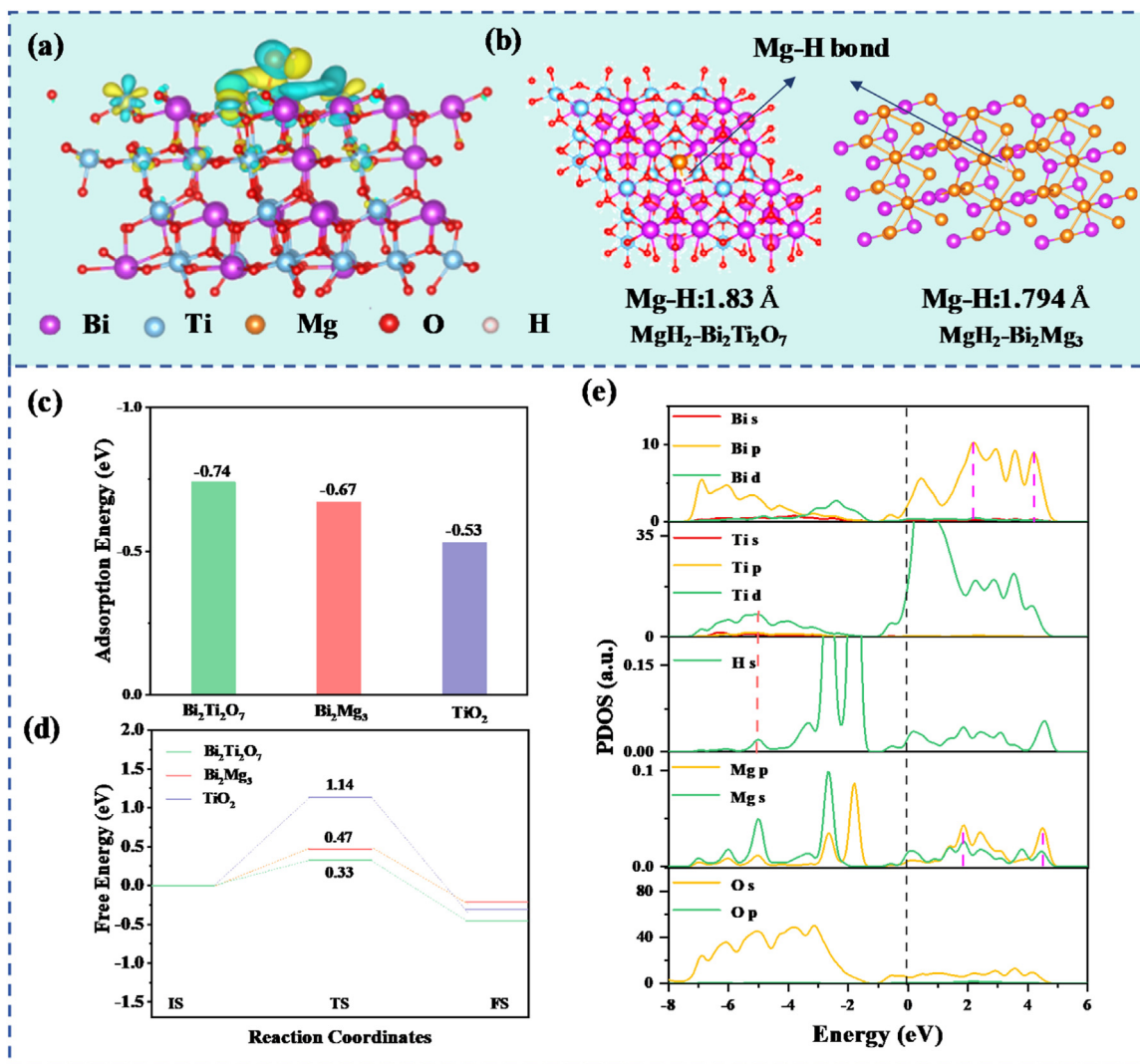


Fig. 7. (a) Optimized structures for  $\text{MgH}_2$  absorbed near  $\text{Bi}_2\text{Ti}_2\text{O}_7$ ; (b) calculated  $\text{Mg}-\text{H}$  bonds on the  $\text{MgH}_2-\text{Bi}_2\text{Ti}_2\text{O}_7$  and  $\text{MgH}_2-\text{Bi}_2\text{Mg}_3$ ; (c) hydrogen dissociation paths and associated activation energies of  $\text{Bi}_2\text{Ti}_2\text{O}_7$ ,  $\text{Bi}_2\text{Mg}_3$  and  $\text{TiO}_2$ ; (d) adsorption energy of  $\text{MgH}_2-\text{Bi}_2\text{Ti}_2\text{O}_7$ ,  $\text{Bi}_2\text{Mg}_3$  and  $\text{MgH}_2-\text{TiO}_2$ ; (e) DOS of the  $\text{MgH}_2-\text{Bi}_2\text{Ti}_2\text{O}_7$  system.

tivity. Figs. S12 and S13 show the optimized structures of  $\text{Bi}_2\text{Ti}_2\text{O}_7$  and  $\text{Bi}_2\text{Mg}_3$  after hydrogen dissociation in different transition states.

The catalytic mechanism of the  $\text{Bi}_2\text{Ti}_2\text{O}_7$  on  $\text{MgH}_2$  can be thoroughly clarified by integrating results from a range of analyses, including XRD, XPS, TEM, SAED, and DFT, offering a more detailed and comprehensive understanding. In pure  $\text{MgH}_2$ , the lack of an electron transfer medium impedes the efficient dissociation of hydrogen molecules. In contrast,  $\text{Bi}_2\text{Ti}_2\text{O}_7$ , a bimetallic oxide, although less stable than the monometallic  $\text{Bi}_2\text{O}_3$ , exhibits high reactivity of the Bi species. This reactivity facilitates its interaction with  $\text{MgH}_2$  during the ball milling process, leading to the formation of the  $\text{Bi}_2\text{Mg}_3$  alloy phase. The *in-situ* formation of this alloy phase effectively enhances the kinetics of the  $\text{MgH}_2$  system, primarily by creating additional hydrogen diffusion channels through the increased number of interfaces. This catalysis lowers the

dehydrogenation temperature and accelerates the overall dehydrogenation kinetics.

Fig. 8 shows the mechanism diagram of the catalytic process.  $\text{MgH}_2-\text{Bi}_2\text{Ti}_2\text{O}_7$  composites formed rich interfaces in the process of hydrogen absorption and discharge reaction, where the multivalent Ti species act as mediators for electron transfer between  $\text{Mg}^{2+}$  and  $\text{H}^-$ . During ball milling, the  $\text{MgH}_2$ -10 wt. %  $\text{Bi}_2\text{Ti}_2\text{O}_7$  sample reacts with  $\text{MgH}_2$ , forming  $\text{TiO}_2$ , which remains present throughout the process. Concurrently, reduction reactions occur, converting a portion of  $\text{Ti}^{4+}$  to  $\text{Ti}^{3+}$  and  $\text{Ti}^0$ . This multivalent titanium-based catalyst not only offers a large number of active catalytic sites through its extensive interaction with  $\text{MgH}_2$  but also facilitates rapid electron transfer and efficient hydrogen atom or molecule diffusion. Moreover, the hollow spherical structure of  $\text{Bi}_2\text{Ti}_2\text{O}_7$ , with its high specific surface area, further contributes to the presence of active sites, enhancing its catalytic performance

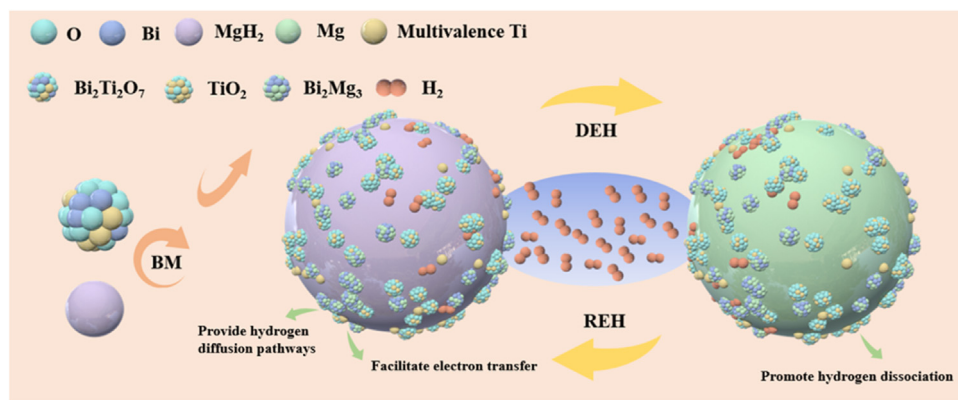


Fig. 8. Catalytic mechanism diagram of  $\text{Bi}_2\text{Ti}_2\text{O}_7$  effect on the hydrogen storage performance of  $\text{MgH}_2$ .

in both the dehydrogenation and hydrogenation reactions of  $\text{MgH}_2$ .

#### 4. Conclusions

In summary, the successful synthesis and application of hollow  $\text{Bi}_2\text{Ti}_2\text{O}_7$  microspheres significantly elevate the hydrogen storage performance of magnesium-based materials. Experimental results reveal that the  $\text{MgH}_2\text{-Bi}_2\text{Ti}_2\text{O}_7$  composite demonstrates superior hydrogen storage capacity compared to the separately mixed  $\text{Bi}_2\text{O}_3$  and  $\text{TiO}_2$  materials. This enhancement can be chiefly due to the synergistic catalytic effect among the constituent elements. The interaction between Bi and  $\text{MgH}_2$  promotes the formation of the  $\text{Bi}_2\text{Mg}_3$  alloy, which accelerates hydrogen diffusion within the  $\text{MgH}_2$ , thereby further improving its catalytic performance. Moreover,  $\text{TiO}_2$  and the multivalent transition metal Ti not only provide catalytic active sites but also facilitate efficient electron transfer. The transition metal oxide functions as an effective buffer, preventing powder agglomeration. As a result, the synergistic effects within the composite material lead to a substantial improvement in hydrogen storage performance. This study not only presents a novel approach to catalyst structural design by enhancing hydrogen adsorption and diffusion facilitated by synergistic catalysis and enhanced surface area but also drives  $\text{MgH}_2$  towards more efficient and stable hydrogen storage, laying the foundation for the wider application of hydrogen energy technologies.

#### Declaration of competing interest

The authors declare that they have no known competing financial interests or personal relationships that could have appeared to influence the work reported in this paper.

#### CRediT authorship contribution statement

**Xiaoying Yang:** Writing – review & editing, Writing – original draft, Visualization, Methodology, Data curation. **Xinqiang Wang:** Writing – review & editing, Visualization, Supervision, Methodology, Investigation, Funding ac-

quisition. **Ruijie Liu:** Writing – review & editing, Methodology, Data curation. **Yanxia Liu:** Methodology, Funding acquisition. **Zhenglong Li:** Methodology, Conceptualization. **Wengang Cui:** Funding acquisition. **Fulai Qi:** Supervision, Funding acquisition. **Yaxiong Yang:** Supervision, Methodology. **Jian Chen:** Funding acquisition, Conceptualization. **Hongge Pan:** Supervision, Methodology, Funding acquisition, Conceptualization.

#### Acknowledgments

The research was supported by the National Key Research and Development Program of China (No. 2024YFB4007204, 2022YFB4004301), the National Natural Science Foundation of China (Grant Nos. 52477220, 52301287, 22005353), the Two-chain Integration Key Project of Shaanxi Province (2021LLRH-09), the Key Research and Development Program of Shaanxi Province (No. 2024CY2-GJHX-44, 2024CY2-GJHX-53, 2024GX-ZDCYL-04-06), the Key Industrial Chain Technology Research Program of Xi'an city (23LL-RHZDZX0017).

#### Supplementary materials

Supplementary material associated with this article can be found, in the online version, at doi:10.1016/j.jma.2025.06.014.

#### References

- [1] X. Zuo, X. Mo, W. Zhou, J. Zhang, C. Hu, W. Jiang, Int. J. Hydrogen Energy 83 (2024) 1309–1319.
- [2] N.A. Ali, N.A. Sazelee, M.F. Md Din, M.M. Nasef, A.A. Jalil, H. Liu, M. Ismail, J. Magnes. Alloys 11 (6) (2023) 2205–2215.
- [3] R. Zou, J.L. Li, W.J. Zhang, G.T. Lei, Z. Li, H.J. Cao, J. Mater. Chem. A 11 (22) (2023) 11748–11754.
- [4] X. Zhang, K. Wang, X. Zhang, J. Hu, M. Gao, H. Pan, Y. Liu, Int. J. Energy Res. 45 (2020) 3129–3141.
- [5] F. Bu, A. Wajid, N. Yang, M. Gu, X. Zhao, L. Huang, X. Ji, S. Ding, Y. Cheng, J. Zhang, J. Mater. Chem. A 12 (20) (2024) 12190–12197.
- [6] L. Chen, X. Liu, L. Zheng, Y. Li, X. Guo, X. Wan, Q. Liu, J. Shang, J. Shui, Appl. Catalysis B: Env. 256 (2019) 117849.
- [7] L. Zhang, Y. Zhang, F. Wu, Y. Jiang, Y. Wang, Inorg. Chem. 62 (14) (2023) 5845–5853.

- [8] M. Chen, Y. Pu, Z. Li, G. Huang, X. Liu, Y. Lu, W. Tang, L. Xu, S. Liu, R. Yu, J. Shui, *Nano. Res.* 13 (8) (2020) 2063–2071.
- [9] Z. Yuan, Y. Wang, X. Zhang, S. Guan, X. Wang, L. Ji, Q. Peng, S. Han, Y. Fan, B. Liu, *Nano. Res.* 17 (8) (2024) 7117–7125.
- [10] L. Zhang, Z. Sun, Z. Yao, L. Yang, N. Yan, X. Lu, B. Xiao, X. Zhu, L. Chen, *Nanosc. Adv.* 2 (2020) 1666–1675.
- [11] J. Zhang, Q. Hou, J. Chang, D. Zhang, Y. Peng, X. Yang, *Solid State Sci.* 121 (2021) 106750.
- [12] Y. Chen, B. Sun, G. Zhang, Y. Wang, X. Li, *Appl. Surf. Sci.* 645 (2024) 158801.
- [13] X. Zhang, Y. Liu, Z. Ren, X. Zhang, J. Hu, Z. Huang, Y. Lu, M. Gao, H. Pan, *Energy Environ. Sci.* 14 (4) (2021) 2302–2313.
- [14] Y. Pang, X. Wan, Y. Li, M. Song, X. Liu, J. Shang, L. Zheng, J.J.A.M. Shui, *Adv. Mater.* 36 (2024) 2412942.
- [15] L. Dan, H. Wang, X. Yang, J. Liu, L. Ouyang, M. Zhu, *ACS Appl. Mater. Interf.* 15 (25) (2023) 30372–30382.
- [16] Z. Yu, X. Liu, Y. Liu, Y. Li, Z. Zhang, K. Chen, S. Han, *Fuel* 357 (2024) 129726.
- [17] S. Ding, Y. Qiao, X. Cai, C. Du, Y. Wen, X. Shen, L. Xu, S. Guo, W. Gao, T. Shen, *J. Magnes. Alloys* 12 (10) (2024) 4278–4288.
- [18] Q. Yuan, C. Peng, C. Yang, Y. Li, Q. Zhang, Y. Lv, G. Liu, D. Liu, *Int. J. Hydrogen Energy* 85 (2024) 12–19.
- [19] Y. Liu, Y. Cao, L. Huang, M. Gao, H. Pan, *J. Alloys Compd.* 509 (3) (2011) 675–686.
- [20] L. Wang, T. Zhong, F. Wu, D. Chen, Z. Yao, L. Chen, L. Zhang, *Chem. Engineer. J.* 505 (2025) 159591.
- [21] L. Sun, R. Sun, J. Liu, M. Zhu, X. Zhang, D. Guo, K. Yin, Z. Zhuang, X. Zhu, P. Xiao, *Nanoscale* 16 (42) (2024) 19873–19880.
- [22] P. Xiao, J. Liu, D. Guo, L. Yang, L. Sun, S. Li, L. Xu, H. Liu, *J. Alloys Compd.* 955 (2023) 170297.
- [23] Q. Luo, J. Li, B. Li, B. Liu, H. Shao, Q. Li, *J. Magnes. Alloys* 7 (1) (2019) 58–71.
- [24] H. Reardon, N. Mazur, D.H. Gregory, *Prog. Natur. Sci.: Mater. Int.* 23 (3) (2013) 343–350.
- [25] C.Q. Zhou, Q.A. Zhang, *J. Alloys Compd.* 804 (2019) 299–304.
- [26] H. Pan, Y. Liu, M. Gao, Y. Zhu, Y. Lei, Q. Wang, *J. Alloys Compd.* 351 (1) (2003) 228–234.
- [27] G. Liang, J. Huot, S. Boily, A. Van Neste, R. Schulz, *J. Alloys Compd.* 292 (1) (1999) 247–252.
- [28] B. Han, J. Wang, J. Tan, Y. Ouyang, Y. Du, L. Sun, *J. Energy Stor.* 83 (2024) 110612.
- [29] K. Xian, M. Wu, M. Gao, S. Wang, Z. Li, P. Gao, Z. Yao, Y. Liu, W. Sun, H. Pan, *Small* 18 (43) (2022) 2107013.
- [30] X. Yang, J. Zhang, Q. Hou, X. Guo, *Nanomaterials (Basel)* 12 (14) (2022) 2468.
- [31] H. Guan, Y. Lu, J. Liu, Y. Ye, Q. Li, F. Pan, *ACS Catal.* 14 (22) (2024) 17159–17170.
- [32] Q. Hou, X. Yang, J. Zhang, W. Yang, E. Lv, *J. Alloys Compd.* 899 (2022) 163314.
- [33] H. Xiao, F. Qian, X. Zhang, H. Hu, R. Tang, C. Hu, W. Zhou, X. He, Z. Pu, C. Ma, R. Wang, L. Yi, Q. Chen, *Chem. Engineer. J.* 494 (2024) 153203.
- [34] Y. Liu, K. Zhong, K. Luo, M. Gao, H. Pan, Q. Wang, *J. Am. Chem. Soc.* 131 (5) (2009) 1862–1870.
- [35] M. Wu, M. Gao, S. Qu, Y. Liu, W. Sun, X. Zhang, C. Liang, X. Zhang, Y. Yang, H. Pan, *J. Magnes. Alloys* 13 (2) (2024) 613–625.
- [36] J.-Q. Hu, W. Jiang, N. Si, Z. Wang, H. Zhang, *Int. J. Hydrogen Energy* 86 (2024) 445–455.
- [37] G. Kresse, J. Hafner, *Phys. Rev. B* 47 (1) (1993) 558–561.
- [38] J.P. Perdew, K. Burke, M. Ernzerhof, *Phys. Rev. Lett.* 77 (18) (1996) 3865–3868.
- [39] G. Kresse, D. Joubert, *Phys. Rev. B* 59 (3) (1999) 1758–1775.
- [40] P.E. Blöchl, *Phys. Rev. B* 50 (24) (1994) 17953–17979.
- [41] G. Liu, L. Wang, Y. Hu, C. Sun, H. Leng, Q. Li, C.J.J.O.A. Wu, *Compounds* 881 (2021) 160644.
- [42] N.A. Ali, N.H. Idris, M.F.M. Din, M.S. Yahya, M. Ismail, *J. Alloys Compd.* 796 (2019) 279–286.
- [43] X. Yang, H. Wan, S. Zhou, Y. Dai, Y.a. Chen, F.S. Pan, *Int. J. Hydrog. Energy* (2023) 27726–27736.
- [44] Q. Meng, Y. Huang, J. Ye, G. Xia, G. Wang, L. Dong, Z. Yang, X. Yu, *J. Alloys Compd.* 851 (2021) 156874.
- [45] S. Guemou, F. Wu, P. Chen, J. Zheng, T. Bian, D. Shang, A.P. Levtssev, L. Zhang, *Int. J. Hydrogen Energy* 48 (62) (2023) 23943–23955.
- [46] H. Gao, R. Shi, Y. Shao, Y. Liu, Y. Zhu, J. Zhang, X. Hu, L. Li, Z. Ba, *J. Alloys Compd.* 895 (2022) 162635.
- [47] Y. Meng, J. Zhang, S. Ju, Y. Yang, Z. Li, F. Fang, D. Sun, G. Xia, H. Pan, X. Yu, *J. Mater. Chem. A* 11 (18) (2023) 9762–9771.
- [48] C. Liang, Y. Fan, Z. Wang, Y. Zhou, M. Zhang, C. Ma, *Int. J. Hydrogen Energy* 96 (2024) 984–994.
- [49] N. Sazelee, M.F. Md Din, M. Ismail, *Materials (Basel)* 16 (6) (2023) 2176.
- [50] T. Huang, Y. Zhao, B. Wang, Y. Li, J. Zhang, X. Wang, Y. Wang, H. Du, M. Fang and J. Zou, *J. Magnes. Alloys*, doi:10.1016/j.jma.2024.11.008.
- [51] X. Chen, C. Peng, Q. Zhang, *Int. J. Hydrogen Energy* 93 (2024) 1474–1486.
- [52] K. Nie, J. Li, H. Lu, R. Zhang, Y.A. Chen, F. Pan, *Sep. Purif. Technol.* 359 (2025) 130839.
- [53] Z. Liu, H. Ning, R. Liu, S. Ding, J. Yang, Y. Tan, Y. Fan, R. Li, P. Qing, H. Liu, J. Guo, Z. Lan, *Chem. Engineer. J.* 499 (2024) 155877.
- [54] X. Huang, X. Xiao, X. Wang, C. Wang, X. Fan, Z. Tang, C. Wang, Q. Wang, L. Chen, *J. Phys. Chem. C* 122 (49) (2018) 27973–27982.
- [55] Y. Pang, X. Wan, Y. Li, M. Song, X. Liu, J. Shang, L. Zheng, J. Shui, *Adv. Mater.* 36 (50) (2024) 2412942.